Accepted Manuscript

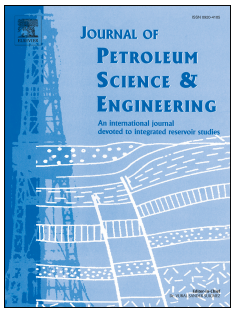

The splicing of backscattered scanning electron microscopy method used on evaluation of microscopic pore characteristics in shale sample and compared with results from other methods

Fangwen Chen, Shuangfang Lu, Xue Ding, Xipeng He, Huilin Xing

PII: S0920-4105(17)30842-2

DOI: 10.1016/j.petrol.2017.10.063

Reference: PETROL 4387

To appear in: *Journal of Petroleum Science and Engineering*

Received Date: 26 June 2017

Revised Date: 21 September 2017

Accepted Date: 24 October 2017

Please cite this article as: Chen, F., Lu, S., Ding, X., He, X., Xing, H., The splicing of backscattered scanning electron microscopy method used on evaluation of microscopic pore characteristics in shale sample and compared with results from other methods, *Journal of Petroleum Science and Engineering* (2017), doi: 10.1016/j.petrol.2017.10.063.

Abstract

The splicing of backscattered scanning electron microscopy (SB-SEM) method was applied to evaluate the microscopic pore characteristics of the Lower Silurian Longmaxi Shale samples from Py1 well in Southeast Chongqing, China. The results from SB-SEM, including frequencies, volumes and specific surface areas of organic and inorganic pores with different sizes, were compared with those of low temperature nitrogen adsorption/desorption (LTNA) and mercury intrusion porosimetry (MIP). The results show that the changes in organic and inorganic surface porosity with increasing image area estimated from the SB-SEM method become almost stable when the SB-SEM image areas are larger than 0.4 mm^2, which indicates that the heterogeneities of organic and inorganic pore volumes in shale samples can be largely overcome. This method is suitable for evaluating the microscopic pore characteristics of shale samples. Although the SB-SEM underestimates the frequencies, volumes and specific surface areas of pores smaller than its resolution, it can obtain these characteristics of pores larger than 100 nm in width, which are not effectively evaluated by the LTNA method and are underestimated by the MIP method.

The splicing of backscattered scanning electron microscopy method used on evaluation of microscopic pore characteristics in shale sample and compared with results from other methods

Fangwen Chen[a, b], Shuangfang Lu[a, *], Xue Ding[a], Xipeng He[c], Huilin Xing[b]

[a] *Research Institute of Unconventional Oil & Gas and Renewable Energy, China University of Petroleum (East China), Qingdao, 266580, China*

[b] *School of Earth and Environmental Sciences, University of Queensland, Brisbane, QLD 4072, Australia*

[c] *Research Institute of Petroleum Exploration and Development, East China Branch, SINOPEC, Nanjing, 210011, China*

Abstract

The splicing of backscattered scanning electron microscopy (SB-SEM) method was applied to evaluate the microscopic pore characteristics of the Lower Silurian Longmaxi Shale samples from Py1 well in Southeast Chongqing, China. The results from SB-SEM, including frequencies, volumes and specific surface areas of organic and inorganic pores with different sizes, were compared with those of low temperature nitrogen adsorption/desorption (LTNA) and mercury intrusion porosimetry (MIP). The results show that the changes in organic and inorganic surface porosity with increasing image area estimated from the SB-SEM method become almost stable when the SB-SEM image areas are larger than 0.4 mm^2, which indicates that the heterogeneities of organic and inorganic pore volumes in shale samples can be largely overcome. This method is suitable for evaluating the microscopic pore characteristics of shale samples. Although the SB-SEM underestimates the frequencies, volumes and specific surface areas of pores smaller than its resolution, it can obtain these characteristics of pores larger than 100 nm in width, which are not effectively evaluated by the LTNA method and are underestimated by the MIP method.

Keywords: microscopic pore; Longmaxi Shale; frequency; pore volume; specific surface area

* Corresponding author.
E-mail address: lusfupc@163.com (S. Lu)

1. Introduction

The pore characteristics of shale reservoir are a focus of research because pore size distributions (including frequencies and volumes of pores with different sizes) and the specific surface areas of nanometer- to micrometer-scale pores have great significance in terms of the storage capacity and flow characteristics of shale gas. At present, the measurement techniques that are used in assessment of the microscopic pore characteristics of shale samples are divided into two categories, namely, radiation and fluid penetration methods (Clarkson et al., 2012).

Radiation methods, including scanning electron microscopy (SEM), field emission scanning electron microscopy, backscatter mode SEM, transmission electron microscopy, three dimension (3D) image reconstruction technology and computed tomography, have provided direct visual observation of microscopic features in shale samples (Jarvie et al., 2007; Slatt and O'Brien, 2011; Zou et al., 2011; Curtis et al., 2012; Loucks et al., 2012). In particular, 3D image reconstruction technology can be used to investigate the shale microstructure and analyze the characteristics of pores (Curtis et al., 2012). For these radiation methods, their higher resolutions correspond to smaller sample sizes (Long et al., 2009), and smaller samples are less representative because of the strong heterogeneity of shale (Slatt and O'Brien, 2011; Curtis et al, 2012).

Fluid penetration methods include low temperature nitrogen adsorption/desorption (LTNA) and mercury intrusion porosimetry (MIP). They refer to injecting a non-wetting fluid into a shale sample and recording the fluid volume and injection pressure. The pore size distribution and specific surface area are then calculated using several theoretical models (Ross and Bustin, 2009; Clarkson et al., 2012, 2013; Li et al., 2015; Okolo et al., 2015). Because of the differences in the experimental environment (temperature and pressure) and the properties of the injected fluids, the LTNA and MIP methods detect different pore size ranges. The nanometer- to micrometer-scale pore systems in shale samples were evaluated by combining the results of them (Clarkson et al. 2012, 2013; Okolo et al. 2015). However, the LTNA and MIP methods only reflect interconnected pores,

as the injected fluids cannot access isolated pore volumes (Bolton et al., 2000; Sigal, 2009; Clarkson et al., 2013; Kuila et al., 2014). In addition, the results of the MIP method reflect the pore volumes connected by throats corresponding to different injection pressures, which are much smaller than the pore sizes (Josh et al., 2012; Kuila and Prasad, 2013; Lin et al., 2015).

Recently, the splicing of backscattered scanning electron microscopy (SB-SEM) method has been used in the evaluation of microscopic pore characteristics of shale samples (Zhang et al., 2017). This method uses matrix backscatter mode scanning performed at high resolution on a polished surface of a shale sample in order to obtain a series of images in rows and columns. Then, those images are assembled to form a relatively large image. This study used the Lower Silurian Longmaxi Shale samples from Py1 well in Southeast Chongqing as an example to evaluate the microscopic pore characteristics of shale samples and compare the results of pore size distributions and specific surface areas with those obtained using other methods, such as LTNA and MIP.

2. Samples and methods

2.1. Samples

Two samples from the Lower Silurian Longmaxi Shale obtained from a key exploratory well (Py1 well) drilled for shale gas exploration in Southeast Chongqing (Fig. 1). Southeast Chongqing has an area of approximately 1.98×10^4 km^2. Hubei Province, Guizhou Province and Hunan Province lie to the north, south and east of Southeast Chongqing. It belongs to the Yangtze tectonic plate and is located in the Wuling Drape Zone and the Western Hunan-Hubei Thrust Belt. The Xuefengshan Uplift and Sichuan Basin lie to the east and northwest of Southeast Chongqing, respectively (Fig. 1). The residual strata of Paleozoic age date to the Cambrian, Ordovician and Silurian, and the other layers are denuded or missing. The Lower Paleozoic marine shales mainly include the Lower Cambrian Niutitang Shale and the Lower Silurian Longmaxi Shale, which are widely deposited in Southeast Chongqing. The Longmaxi Shale has yielded shale gas from all of the exploratory wells that have been drilled for shale gas exploration, such as Py1, Yy1, Jq1 and

Ny1 (Fig. 1), and commercial gas flow has been obtained from several wells, including Py1 well. It indicates that the Longmaxi Shale in Southeast Chongqing has a good exploration potential for shale gas. The sample no. 1 is mudstone and the other is carbonaceous shale, which are typical of marine shale found in southern China (Fig. 1). Geochemical characteristics and geological features of the samples, such as total organic carbon (*TOC*), Rock-Eval parameters (S_1, S_2, and T_{max}), vitrinite reflectance (R_o), element of organic matter (*C*, *H*, *O*, *N* and *S*), porosity from the Gas Research Institute (GRI) method, and mineral composition are shown in Table 1 and Table 2.

2.2. LTNA

The low temperature N_2 adsorption/desorption (LTNA) measurements were performed using an ASAP 2020 Micropore Physisorption Analyzer to measure the pore size distributions and specific surface areas of the shale samples. Approximately 200-500 mg of crushed sample (60-80 mesh) was preheated in a vacuum oven at 80 °C for 12-16 hours to remove all pore fluids, such as water, oil and adsorbed gas. Reagent-grade nitrogen (99.999%) was used as the adsorbate at -196.15 °C. The adsorption-desorption isotherms were achieved from recording the adsorption and desorption volumes under relative pressures ranging from 0.01 to 1, and the equilibration time was set as 10 s. Pore size distributions were obtained from the adsorption isotherms using the density functional theory (DFT) method, assuming cylindrical pores (Seaton and Walton, 1989; Lastoskie et al., 1993; Zhang and Yang, 2013). Pore volumes were obtained using the Barrette Joynere Halenda (BJH) method (Gregg and Sing, 1982), and specific surface areas were calculated using the Brunauer Emmette Teller (BET) method.

2.3. MIP

Mercury intrusion porosimetry (MIP) is a technique that is widely used in measuring pore size distribution (Kate and Gokhale, 2006; Cao et al., 2015; Wang et al., 2015). The experiments were performed using a Micromeritics AutoPore IV 9500, which has the ability to reach pressure up to approximately 413.7 MPa or 600000 psi, representing a pore throat size of approximately 3 nm

(Clarkson et al., 2013; Kuila et al., 2014). Before the experiments, the cylindrical plug core samples (diameter of approximately 2.5 cm) were dried for 15 hours at 110 °C in a vacuum drying oven to drive off any physically adsorbed water. The intrusion and extrusion curves were obtained from recording the volumes of mercury injected and ejected under different pressures during the process of increasing the pressure up to approximately 120 MPa and reversed by decreasing the pressure stepwise. The pore radius corresponding to the pressure was calculated using the Washburn Equation (Eq. (1)). The pore frequencies, volumes and specific surface areas of different pore sizes could be calculated using Eq. (2), (3) and (4).

$$r_i = (-2\sigma\cos\theta)/P_i \quad (1)$$

$$F_{MIP\text{-}i} = \frac{V_i}{r_i^3}/(\sum_{j=1}^{n}\frac{V_j}{r_j^3})\times 100\% \quad (2)$$

$$\Phi_{MIP\text{-}i}=V_i/V\times 100\% \quad (3)$$

$$SSA_{MIP\text{-}i}=2V_i/(r_i\cdot M) \quad (4)$$

where r_i is the pore radius (μm) when mercury just accesses under the i^{th} pressure P_i (MPa). σ is the interfacial tension of mercury, which is 0.48 J/m^2 in the MIP experiment. θ is the contact angle between mercury and the pore surface, which is 140 º in the MIP experiment (Kate and Gokhale, 2006; Cao et al., 2015; Wang et al., 2015). $F_{MIP\text{-}i}$ is the pore frequency in the i^{th} size range (%). V_i (cm^3) is the volume of mercury injected under the i^{th} pressure P_i. $\Phi_{MIP\text{-}i}$ is the volume ratio of pores in the i^{th} size range and shale sample (%). V is the volume of sample (cm^3). $SSA_{MIP\text{-}i}$ is the special surface area of pores in the i^{th} size range (m^2/g). M is the mass of shale sample (g).

2.4. SB-SEM

2.4.1. Experimental setup

The SB-SEM method applies matrix backscatter mode scanning at high resolution to a polished surface of a shale sample to obtain a series of equally spaced images with overlapping edges arranged in a series of rows and columns. The polished surface is perpendicular to the horizontal plane. Those images are then assembled to become a relatively large image with high resolution.

The operating procedures of the SB-SEM experiment were shown in Fig. 2. For each sub sample (the sub samples are cylindrical and have a diameter of 25 mm and a width of 2-5 mm), a surface approximately 5 mm in length and 3 mm in height was polished by argon-ion method to produce a smooth surface using a Hitachi Ion Milling System IM 4000 with an accelerating voltage of 3 kV. Then, the smooth surface was coated with carbon powder (10 nm in thickness) for the purpose of obtaining a conductive surface without charging. After these pretreatments, the images (55×55 matrix) were obtained from each sample using a Helios NanoLab 650 instrument with a voltage of 10 kV, a beam value of 10 pA and a resolution of 10 nm.

2.4.2. Models for evaluating organic pore volume and specific surface area

Although the microscopic pore structure in shale reservoir is strongly heterogeneous, this issue will be gradually overcome as the number or the total area of high-resolution SB-SEM images increases. When the number (or the total area) reaches a certain value, the frequencies, volumes and specific surface areas of organic pores with different sizes in shale samples will tend to be stable, which will be discussed in Section 3.3. Based on this assumption, models for evaluating the volumes and specific surface areas of organic pores with different sizes in shale samples were established using the results from the SB-SEM method. The area ratio of organic pores and organic matter grains was obtained by identifying the organic pores and organic matter grains in the SB-SEM images. Combined with the total organic carbon, the carbon element weight percentage in organic matter, the organic matter density and the rock density, the area ratio of organic pores and organic matter grains in 2D was converted to a volume ratio of organic pores in shale sample. The volumes of organic pores with different sizes were calculated using Eq. (5) (Chen et al., 2014; Gu et al., 2015). The organic matter content of shale sample was calculated using Eq. (6), which is the result of *TOC* value divided by carbon element weight percentage in *OM*.

$$\Phi_{\text{organic-i}} = \frac{\sum_{1}^{n} S_{\Phi\text{organic-i}}}{\sum_{1}^{n} S_{\text{organic}}} \times \frac{\rho_{\text{rock}} OM}{\rho_{\text{organic}}} \times 100\% \quad (5)$$

$$OM = TOC / C_{\text{OM}} \times 100\% \quad (6)$$

where $\Phi_{\text{organic-i}}$ is the volume ratio of organic pores in the shale sample, and the organic pores are in the i$^{\text{th}}$ size range (%). $S_{\Phi\text{organic-i}}$ is the area of organic pores in the i$^{\text{th}}$ size range (m^2). S_{organic} is the area of organic matter grains (m^2). n is the number of SB-SEM images. OM is the organic matter content of shale sample (%). ρ_{organic} is the density of organic matter, and it is approximately 1.2 g/cm^3 (Okiongbo et al., 2005). ρ_{rock} is the density of rock (g/cm^3). C_{OM} is the carbon element weight percentage in OM (%).

The ratio of organic pore perimeters and organic matter grain areas was also obtained by identifying the organic pores and organic matter grains in the SB-SEM images. Combined with the organic matter content and the organic matter density, the specific surface areas of organic pores with different sizes were calculated using Eq. (7).

$$SSA_{\text{organic-i}} = \frac{\sum_{1}^{n} L_{\Phi\text{organic-i}}}{\sum_{1}^{n} S_{\text{organic}}} \times \frac{OM}{\rho_{\text{organic}}} \quad (7)$$

where $SSA_{\text{organic-i}}$ is the specific surface area of organic pores (m^2/g), and the organic pores are in the i$^{\text{th}}$ size range. $L_{\Phi\text{organic-i}}$ is the perimeter of organic pores in the i$^{\text{th}}$ size range (m).

2.4.3. Models for evaluating inorganic pore volume and specific surface area

In the same way, the area ratio of inorganic pores and inorganic matrixes was obtained by identifying the inorganic pores in the SB-SEM images. Combined with the percent inorganic matrix content, the inorganic matrix density and the rock density, the area ratio of inorganic pores and inorganic matrixes in 2D was converted to a volume ratio of inorganic pores in shale sample. The volumes of inorganic pores with different sizes were calculated using Eq. (8) (Chen et al., 2014; Gu

et al., 2015). The inorganic matrix density was calculated using Eq. (9).

$$\Phi_{\text{inorganic-i}} = \frac{\sum_{1}^{n} S_{\Phi\text{inorganic-i}}}{\sum_{1}^{n} S_{\text{inorganic}}} \times \frac{\rho_{\text{rock}} \times (1 - OM)}{\rho_{\text{inorganic}}} \times 100\% \quad (8)$$

$$\rho_{\text{inorganic}} = \frac{\rho_{\text{organic}} \rho_{\text{rock}} (1 - OM)}{\rho_{\text{organic}} - \rho_{\text{rock}} OM} \quad (9)$$

where $\Phi_{\text{inorganic-i}}$ is the volume ratio of inorganic pores in the shale sample (%), and the inorganic pores are in the i$^{\text{th}}$ size range. $S_{\Phi\text{inorganic-i}}$ is the area of inorganic pores in the i$^{\text{th}}$ size range (m^2). $S_{\text{inorganic}}$ is the area of inorganic matrixes, which is equal to the difference between the image area and the organic matter grain area (m^2). $\rho_{\text{inorganic}}$ is the density of inorganic matrix (g/cm^3).

The ratio of inorganic pore perimeters and inorganic matrix areas was obtained by identifying the inorganic pores in the SB-SEM images. Combined with the inorganic matrix content and inorganic matrix density, the specific surface areas of inorganic pores with different sizes were calculated using Eq. (10).

$$SSA_{\text{inorganic-i}} = \frac{\sum_{1}^{n} L_{\Phi\text{inorganic-i}}}{\sum_{1}^{n} S_{\text{inorganic}}} \times \frac{1 - OM}{\rho_{\text{inorganic}}} \quad (10)$$

where $SSA_{\text{inorganic-i}}$ is the specific surface area of inorganic pores (m^2/g), and the inorganic pores are in the i$^{\text{th}}$ size range. $L_{\Phi\text{inorganic-i}}$ is the perimeter of inorganic pores in the i$^{\text{th}}$ size range (m).

3. Results

3.1. LTNA

Because pores are connected by throats and pore sizes are much larger than throat sizes, the hysteresis loops are common in shale samples. According to the IUPAC classification (Sing et al., 1985), the hysteresis loops of the two samples belong to type H3 (Fig. 3a and b). It suggests that the slit and wedge-shaped pores are developed in the two samples. Moreover, the adsorbed N_2

quantities of sample no. 2 at the minimum and maximum relative pressures are all higher than those of sample no. 1, indicating that the small pore volume and total pore volume in sample no. 2 are more developed than those of sample no. 1, which is also reflected by the pore size distributions obtained using the BJH and DFT models (Fig. 3c and d). The volumes of pores with different sizes from the BJH model are larger than those of DFT model. The trends in pore size distribution from the two models are consistent when the pore size is larger than 3 nm. However, for pore sizes smaller than 3 nm, the pore volumes calculated using the BJH model increase obviously with decreasing pore size, and the pore volumes calculated using the DFT model decrease with decreasing pore size. In addition, the pore size distributions using the DFT model have multiple peaks, which may prefer to describe the pore size distribution of small pores, such as micropores or narrow mesopores (Li et al., 2015). The BJH model is more suitable for measuring mesopores rather than micropores (Wang et al., 2014), so the results from BJH model are unreliable while pore sizes smaller than 3 nm. At the same time, the precision of DFT model was greatly improved because the density distribution of adsorption layer was corrected (Seaton and Walton, 1989; Lastoskie et al., 1993).

3.2. MIP

The relationships between the injected/ejected mercury saturation/cumulative porosity and pore width of the two shale samples were shown in Fig. 4. The values of max saturation and cumulative porosity from the two samples are 31.15 %, 0.56 % and 45.34 %, 1.02 %. The mercury obviously accessed into the pore systems of the two samples while the pore width is smaller than 5 μm and quickly injected into the pore systems while the pore width is smaller than 100 nm. The pore sizes of the dominated pore volumes in the two samples are both smaller than 100 nm (Fig. 4).

3.3. SB-SEM

The composite images, local images and single scan images obtained from the two shale samples using the SB-SEM method are shown in Fig. 5. The size of each composite image is

1.014×0.875 mm^2, and each composite image is composed of 3025 individual images (55×55). The size of each local image is 0.1232×0.0921 mm^2, and each local image contains 42 individual images (6×7) and is marked by a red rectangle in the composite image. The size of a single scan image is 0.02×0.0173 mm^2. Inorganic pores, organic pores, organic matter grains and several minerals were identified in these images, which were taken at multiple scales.

To determine how many SB-SEM images or areas are needed to largely overcome the heterogeneity of pore volume in shale sample, the parameters of the two shale samples, such as the perimeters and areas of organic and inorganic pores, as well as the areas of organic matter grains and images, were identified and analyzed based on the SB-SEM images. The organic and inorganic surface porosity values were calculated using Eq. (5) and Eq. (8). The changes in organic and inorganic surface porosity values with the areas of SB-SEM images show that, when the SB-SEM image areas are smaller than 0.4 mm^2, the changes in organic and inorganic surface porosity values clearly fluctuate with areas of images. In addition, the surface porosity values become almost stable while the image areas are bigger than 0.4 mm^2 (Fig. 6). This shows that the heterogeneities of organic and inorganic pore volumes in the two shale samples can be largely overcome when the SB-SEM image areas are bigger than 0.4 mm^2 on the basis of the limited data available. So the results of frequencies, volumes and specific surface areas of organic and inorganic pores with different sizes in the two shale samples from SB-SEM method are relatively credible while the SB-SEM image areas are bigger than 0.4 mm^2.

4. Discussion

4.1. Comparison of pore frequencies with those of other methods

The frequencies of pores with different sizes determined using the SB-SEM, LTNA and MIP methods show that the number of pores smaller than 50 nm in width is dominant in the pore size range of 0-400 nm, and the pore frequency decreases with increasing pore size (Fig. 7). The frequencies of organic and inorganic pores with different sizes (Fig. 7a and b), as well as the

frequencies of pores with different sizes (Fig. 7c and d), were calculated by the SB-SEM method. The organic pores are mainly distributed within the relatively small pore size range, whereas the inorganic pores are mainly distributed in relatively large pore size range. The number of organic pores is absolutely dominant. The SB-SEM underestimates the number of pores smaller than 20 nm in width, because the pores have sizes that are smaller than or close to the resolution of SB-SEM images. The pores identified using the SB-SEM method mainly concentrate in the pore width range smaller than 150 nm, and the pore frequency gradually decreases with increasing pore size (Fig. 7c and d). The pore frequencies obtained using the LTNA (Fig. 7e and f) and MIP (Fig. 7g and h) methods are very similar. The pores identified by the LTNA and MIP methods mainly concentrate in the pore width range smaller than 50 nm. The pore frequency quickly decreases with increasing pore size, and the decreasing trends are much more obvious than those revealed by the SB-SEM method.

Although the SB-SEM method underestimates the number of pores smaller than 20 nm in width, it can evaluate the frequencies of pores larger than 100 nm in width, which are not effectively evaluated by the LTNA method and are underestimated by the MIP method. The process of crushing sample for the LTNA measurement creates some concave and convex surfaces that do not exist in the original sample and affect the result. In addition, the precision of LTNA method is significantly reduced for pores that are larger than 100 nm in width and it is not suitable for measuring pores larger than 100 nm in width (Li et al., 2015). The MIP method measures the volumes of throats and pores connected by throats at different pressures. When calculating the frequencies, volumes and specific surface areas of pores, the volumes of throats and pores were considered as the volumes of throats (Josh et al., 2012; Kuila and Prasad, 2013; Lin et al., 2015), which are much smaller than the corresponding pores. The MIP method inevitably overestimates the frequencies, volumes and specific surface areas of small pores, and underestimates those of relatively large pores.

4.2. Comparison of pore volumes with those of other methods

The volumes of pores with different sizes obtained using the SB-SEM, LTNA and MIP methods show that pore volume decreases with increasing pore size (Fig. 8). The volumes of organic and inorganic pores with different sizes (Fig. 8a and b), as well as the volumes of pores with different sizes (Fig. 8c and d), were measured using the SB-SEM method. The volumes of organic and inorganic pores with different sizes show approximately normal distributions. The volumes of organic pores are mainly concentrated in a relatively small pore size range, whereas the volumes of inorganic pores are mainly concentrated in a relatively large pore size range. The pore volume boundary values between the dominant volume of organic and inorganic pores of the two shale samples correspond to approximately 50 nm and 100 nm in pore width, respectively. The pore volume from the SB-SEM method decreases with increasing pore size in the range of 50-400 nm (Fig. 8c and d). At the same time, the SB-SEM method underestimates the pore volume. The reason is that the SB-SEM method identifies pores from 2D images, and it is difficult to identify the pores when their long axes are almost parallel to the surface of image. The pore volume results from the LTNA (Fig. 8e and f) and MIP (Fig. 8g and h) methods are very similar in the pore width range smaller than 400nm. The pore volumes measured by the LTNA and MIP methods are mainly concentrated in the pore width range smaller than 50 nm. The pore volume quickly decreases with increasing pore size, and the decreasing trends are much more obvious than those of the SB-SEM method.

Compared with the results of the LTNA and MIP methods, the SB-SEM method underestimates the volumes of pores smaller than 20 nm in width. As discussed in section 4.1, the LTNA and MIP methods systematically overestimate the volumes of pores smaller than 20 nm in width. For shale sample, the SB-SEM method is available to measure the volumes of pores larger than 100 nm in width, which are not effectively evaluated by the LTNA method and are underestimated by the MIP method.

4.3. Comparison of specific surface areas with those of other methods

The specific surface areas of pores with different sizes obtained using these methods show that the specific surface area decreases with increasing pore size (Fig. 9). The specific surface areas of organic and inorganic pores with different sizes (Fig. 9a and b), as well as the specific surface areas of pores with different sizes (Fig. 9c and d), were measured using the SB-SEM method. The specific surface areas of organic and inorganic pores with different sizes show approximately normal distributions. The specific surface areas of organic pores are mainly concentrated in a relatively small pore size range, while the specific surface areas of inorganic pores are mainly concentrated in a relatively large pore size range. The specific surface area boundary values between the dominant specific surface areas of organic and inorganic pores of the two shale samples correspond to approximately 50 nm and 100 nm in pore width, respectively. The specific surface area from the SB-SEM method gradually decreases with increasing pore size (Fig. 9c and d). The specific surface areas obtained using the LTNA method (Fig. 9e and f) and the MIP method (Fig. 9g and h) are similar, which are mainly concentrated in the pore width range smaller than 50 nm. The specific surface area quickly decreases with increasing pore size, and the decreasing trends are much more obvious than those obtained using the SB-SEM method.

Compared with the results from the LTNA and MIP methods, the SB-SEM method underestimates the specific surface areas of pores smaller than 20 nm in width. As discussed in section 4.1, the LTNA and MIP methods overestimate the specific surface areas contributed by small pores and miss or underestimate the specific surface areas of relatively large pore size range. The SB-SEM method is suitable to evaluate the specific surface areas of pores larger than 100 nm in width, which are not effectively evaluated by the LTNA method and are underestimated by the MIP method.

4.4. Advantages and disadvantages of the SB-SEM method

The benefits of the SB-SEM method include: (i) it uses radiation method to directly obtain the characteristics of organic and inorganic pores, such as the frequencies, volumes and specific surface

areas of pore with different sizes, and the results of quantitative evaluation are highly reliable; (ii) the heterogeneities of organic and inorganic pore volumes in shale samples are nearly overcome by using the SB-SEM method; and (iii) it is suitable to distinguish organic and inorganic pores in shale samples and evaluate the specific surface areas of pores larger than 100 nm in width that are not effectively evaluated by the LTNA method and are underestimated by the MIP method. The LTNA and MIP methods cannot distinguish and evaluate inorganic and organic pores. The LTNA method can quantitatively evaluate the characteristics of pores smaller than 100 nm in three-dimension and its precision obviously decreases for the pores larger than 100 nm. The MIP method can quantitatively evaluate the full scale of pores including micro-fracture and nano-scale pores in three-dimension. It inevitably overestimates the frequencies, volumes and specific surface areas of small pores, and underestimates those of relatively large pores.

The SB-SEM method has two disadvantages. The first one is that it cannot evaluate the full range of pore sizes. The method cannot identify the pores smaller than the resolution of SB-SEM image and has difficulty in recognizing pores with sizes close to the resolution. The pore size range that can be effectively evaluated using the SB-SEM method is determined by the resolution/ magnification time of single image, the total area of spliced image and the observation position. The other disadvantage is that the pores are identified from 2D images in the SB-SEM method. It is difficult for the SB-SEM method to identify the pores when the long axes of pores and the direction of 2D image are almost parallel.

5. Conclusions

The changes in organic and inorganic surface porosity with image area from the Longmaxi Shale samples become almost stable when the SB-SEM image areas are larger than 0.4 mm^2. It indicates that the heterogeneities of organic and inorganic pore volumes in shale samples can be nearly overcome while the SB-SEM image areas are larger than 0.4 mm^2. The SB-SEM method is suitable for evaluating the frequencies, volumes and specific surface areas of organic and inorganic

pores with different sizes in shale samples.

Compared with the results of the LTNA and MIP methods, the SB-SEM method underestimates the frequencies, volumes and specific surface areas of pores smaller than 20 nm in width. However, it is available to evaluate these characteristics of pores larger than 100 nm in width, which are not effectively evaluated by the LTNA method and are underestimated by the MIP method.

Acknowledgments

This work was supported by the National Natural Science Foundation of China (Grant No. 41530315, 41330313, 41302101), the China Scholarship Council (201606455008), the National Science and Technology Major Project of China (2016ZX05061), the Natural Science Foundation of Shandong Province (ZR2016DL07) and the Fundamental Research Funds for the Central Universities (17CX05012).

Nomenclature

R_o Vitrinite reflectance, %

S_0 Gaseous hydrocarbon, mg/g

S_1 Free hydrocarbon quantity, mg/g

S_2 Pyrolysis hydrocarbon quantity from kerogen, mg/g

T_{max} Peak temperature of pyrolysis hydrocarbon, ºC

r_i Pore radius, μm

σ Interfacial tension of mercury, 0.48 J/m^2

θ Contact angle between mercury and the pore surface, º

P_i Mercury injection pressure, MPa

$F_{MIP\text{-}i}$ Pore frequency in the ith size range, %

V_i Volume of mercury injected under the ith pressure P_i, cm^3

V Volume of sample (cm^3)

$\Phi_{MIP\text{-}i}$ Volume ratio of pores in the ith size range and shale sample, %

$SSA_{MIP\text{-}i}$ Special surface area of pores in the i^{th} size range, m^2/g

M Mass of shale sample, g

$\Phi_{organic\text{-}i}$ Volume ratio of organic pores in the i^{th} size range and shale sample, %

$S_{\Phi organic\text{-}i}$ Area of organic pores in the i^{th} size range, m^2

$S_{organic}$ Area of organic matter grains, m^2

n Number of SB-SEM images

$\rho_{organic}$ Density of organic matter, g/cm^3

$\rho_{inorganic}$ Density of inorganic matrix, g/cm^3

ρ_{rock} Density of rock, g/cm^3

C_{OM} Carbon element weight percentage in organic matter, %

$SSA_{organic\text{-}i}$ Specific surface area of organic pores in the i^{th} size range, m^2/g

$L_{\Phi organic\text{-}i}$ Perimeter of organic pores in the i^{th} size range, m

$\Phi_{inorganic\text{-}i}$ Volume ratio of inorganic pore in the i^{th} size range and shale sample, %

$S_{\Phi inorganic\text{-}i}$ Area of inorganic pores in the i^{th} size range, m^2

$S_{inorganic}$ Area of inorganic matrix, m^2

$SSA_{inorganic\text{-}i}$ Specific surface area of inorganic pore in the i^{th} size range, m^2/g

$L_{\Phi inorganic\text{-}i}$ Perimeter of inorganic pore in the i^{th} size range, m

TOC Total organic carbon content, %

OM Organic matter content, %

Abbreviations

SB-SEM Splicing of backscattered scanning electron microscopy

LTNA Low temperature nitrogen adsorption/desorption

MIP Mercury intrusion porosimetry

SEM Scanning electron microscopy

GRI Gas Research Institute

3D	Three dimension
2D	Two dimension
DFT	Density functional theory
BJH	Barrette Joynere Halenda
BET	Brunauer Emmette Teller

References

Bolton, A.J., Maltmn, A.J., Fisher, Q., 2000. Anisotropic permeability and bimodal pore-size distributions of fine-grained marine sediments. Mar. Pet. Geol. 17(6), 657-672.

Cao, T.T., Song, Z.G., Wang, S.B., Cao, X.X., Li, Y., Xia, J., 2015. Characterizing the pore structure in the Silurian and Permian shales of the Sichuan Basin, China. Mar. Pet. Geol. 61, 140-150.

Chen, F.W., Lu, S.F., Ding, X., 2014. Organoporosity Evaluation of Shale: A Case Study of the Lower Silurian Longmaxi Shale in Southeast Chongqing, China. Scientific World Journal 893520, 9.

Clarkson, C.R., Freeman, M., He, L., Agamalian, M., Melnichenko, Y.B., Mastalerz, M., Bustin, R.M., Radlin´ski, A.P., Blach, T.P., 2012. Characterization of tight gas reservoir pore structure using USANS/SANS and gas adsorption analysis. Fuel 95, 371-385.

Clarkson, C.R., Solano, N., Bustin, R.M., Bustin, A.M.M., Chalmers, G.R.L., He, L., Melnichenko, Y.B., Radlinski, A.P., Blach, T.P., 2013. Pore structure characterization of North American shale gas reservoirs using USANS/SANS, gas adsorption, and mercury intrusion. Fuel 103, 606-616.

Curtis, M.E., Sondergeld, C.H., Ambrose, R.J., Rai, C.S., 2012. Microstructural investigation of gas shales in two and three dimensions using nanometer-scale resolution imaging. AAPG Bull. 96(4), 665-677.

Gregg, S.J., Sing, K.S.W., 1982. Adsorption, Surface Area and Porosity. Academic Press, London, p.

303.

Gu, X., Cole, D.R., Rother, G., Mildner, D.F.R., Brantley, S.L., 2015. Pores in marcellus shale: a neutron scattering and FIB-SEM study. Energy Fuels 29(3), 1295-1308.

Jarvie, D.M., Hill, R.J., Ruble, T.E., Pollastro, R.M., 2007. Unconventional shale-gas systems: the Mississippian Barnett shale of north-central Texas as one model for thermogenic shale-gas assessment. AAPG Bull. 91(4), 475-499.

Josh, M., Esteban, L., Delle, Piane, C., Sarout, J., Dewhurst, D.N., Clennell, M.B., 2012. Laboratory characterization of shale properties. J. Petrol. Sci. Eng. 88-89,107-124.

Kate, J.M., Gokhale, C.S., 2006. A simple method to estimate complete pore size distribution of rocks. Eng. Geol. 84, 48-69.

Kuila, U., McCarty, D.K., Arkadiusz, D., Fischer, T.B., Prasad, M., 2014. Total porosity measurement in gas shales by the water immersion porosimetry (WIP) method. Fuel 117, 1115-1129.

Kuila, U., Prasad, M., 2013. Specific surface area and pore-size distribution in clays and shales. Geophys. Prospect. 61, 341-362.

Lastoskie, C., Gubbins, K.E., Quirke, N., 1993. Pore size distribution analysis of microporous carbons: a density functional theory approach. J. Phys. Chem. 97, 4786-4796.

Li, J.J, Yin, J.X., Zhang, Y.N., Lu, S.F., Wang, W.M., Li, J.B., Chen, F.W., Meng, Y.L., 2015. A comparison of experimental methods for describing shale pore features — A case study in the Bohai Bay Basin of eastern China. Int. J. Coal. Geol. 152, 39-49.

Lin, B., Chen, M., Jin, Y., Pang, H., 2015. Modeling pore size distribution of southern Sichuan shale gas reservoirs. J. Nat. Gas Sci. Eng. 26, 883-894

Long, H., Swennen, R., Foubert, A., Dierick, M., Jacobs, P., 2009. 3D quantification of mineral components and porosity distribution in Westphalian C sandstone by microfocus X-ray computed tomography. Sediment. Geol. 220, 116-125.

Loucks, R.G., Reed, R.M., Ruppel, S.C., Hammes, U., 2012. Spectrum of pore types and networks inmudrocks and a descriptive classification for matrix-relatedmudrock pores. AAPG Bull. 96(6), 1071-1098.

Okiongbo, K.S., Aplin, A.C., Larter, S.R., 2005. Changes in type II Kerogen density as a function of maturity: evidence from the Kimmeridge clay formation. *Energy Fuels*, 19(6), 2495–2499.

Okolo, G.N., Everson, R.C., Neomagus, H.W., Roberts, M.J., Sakurovs, R., 2015. Comparing the porosity and surface areas of coal as measured by gas adsorption,mercury intrusion and SAXS techniques. Fuel 141, 293-304.

Ross, D.J.K., Bustin, R.M., 2009. The importance of shale composition and pore structure upon gas storage potential of shale gas reservoirs. Mar. Pet. Geol. 26(6), 916-927.

Seaton, N.A., Walton, J., 1989. A new analysis method for the determination of the pore size distribution of porous carbons from nitrogen adsorption measurements. Carbon 27(6), 853-861.

Sigal, R.F., 2009. A methodology for blank and conformance corrections for high pressure mercury porosimetry. Meas. Sci. Technol. 20, 1-11.

Sing, K.S.W., Everett, D.H., Haul, R.A.W., Moscou, L., Pierotti, R.A., Rouquerol, J., Siemieniewska, T., 1985. Reporting physisorption data for gas/solid systems with special reference to the determination of surface and porosity. Pure Appl. Chem. 57(4), 603-619.

Slatt, R.M., O'Brien, N.R., 2011. Pore types in the Barnett and Woodford gas shales: Contribution to understanding gas storage and migration pathways in fine-grained rocks. AAPG Bull. 95(12), 2017-2030.

Wang, G.C., Ju, Y.W., Yan, Z.F., Li, Q.G., 2015. Pore structure characteristics of coal-bearing shale using fluid invasion methods: A case study in the Huainan-Huaibei Coalfield in China. Mar. Pet. Geol. 62, 1-13.

Wang, G.D., Wang, K., Ren, T.X., 2014. Improved analytic methods for coal surface area and pore

size distribution determination using 77 K nitrogen adsorption experiment. Int. J. Min. Sci. Technol. 24(3), 329-334.

Zhang, P.F., Lu, S.F., Li, J.Q., Xue, H.T., Li, W.H., Zhang, P., 2017. Characterization of shale pore system: A case study of Paleogene Xin'gouzui Formation in the Jianghan basin, China. Mar. Pet. Geol. 79, 321-334.

Zhang, Z., Yang, Z., 2013. Theoretical and practical discussion of measurement accuracy for physisorption with micro- and mesoporous materials. Chin. J. Catal. 34(10), 1797-1810.

Zou, C.N., Zhu, R.K., Bai, B., Yang, Z., Wu, S.T., Su, L., Dong, D.Z., Li, X.J., 2011. First discovery of nano-pore throat in oil and gas reservoir in China and its scientific value. Acta Petrol. Sin. 27(6), 1857-1864.

Table 1

The base geological and geochemical characteristics of the shale samples.

Sample no.	Depth (m)	R_o (%)	*TOC* (%)	T_{max} (°C)	S_0 (mg/g)	S_1 (mg/g)	S_2 (mg/g)	Element of *OM* (wt. %)					Bulk density (cm^3/g)	Grain density (cm^3/g)	GRI porosity (%)
								C	*H*	*O*	*N*	*S*			
1	2079.92	2.70	1.3	323.3	0.0013	0.0004	0.0035	85.57	1.96	6.39	2.42	3.66	2.71	2.76	1.81
2	2156.75	2.79	3.89	361.7	0.004	0.0085	0.0238	86.19	1.54	7.24	2.30	2.73	2.60	2.66	2.26

Table 2

The mineral compositions of the shale samples.

Sample no.	Whole-rock mineral compositions (%)								Relative clay mineral content (%)			
	Clay	Quartz	Feldspar	Calcite	Dolomite	Aragonite	Pyrite	Barite	Illite	Chlorite	I/S [a]	%S [b]
1	45.5	31.1	9.8	3.1	/	4.7	3.0	2.8	45	13	42	5
2	42.5	30.8	10.9	0.3	5.8	/	8.7	1.0	64	12	24	5

[a] I/S is the weight percentage of illite-smectite mixed-layer in clay minerals.

[b] %S represents the weight percentage of smectite in the illite-smectite mixed-layer.

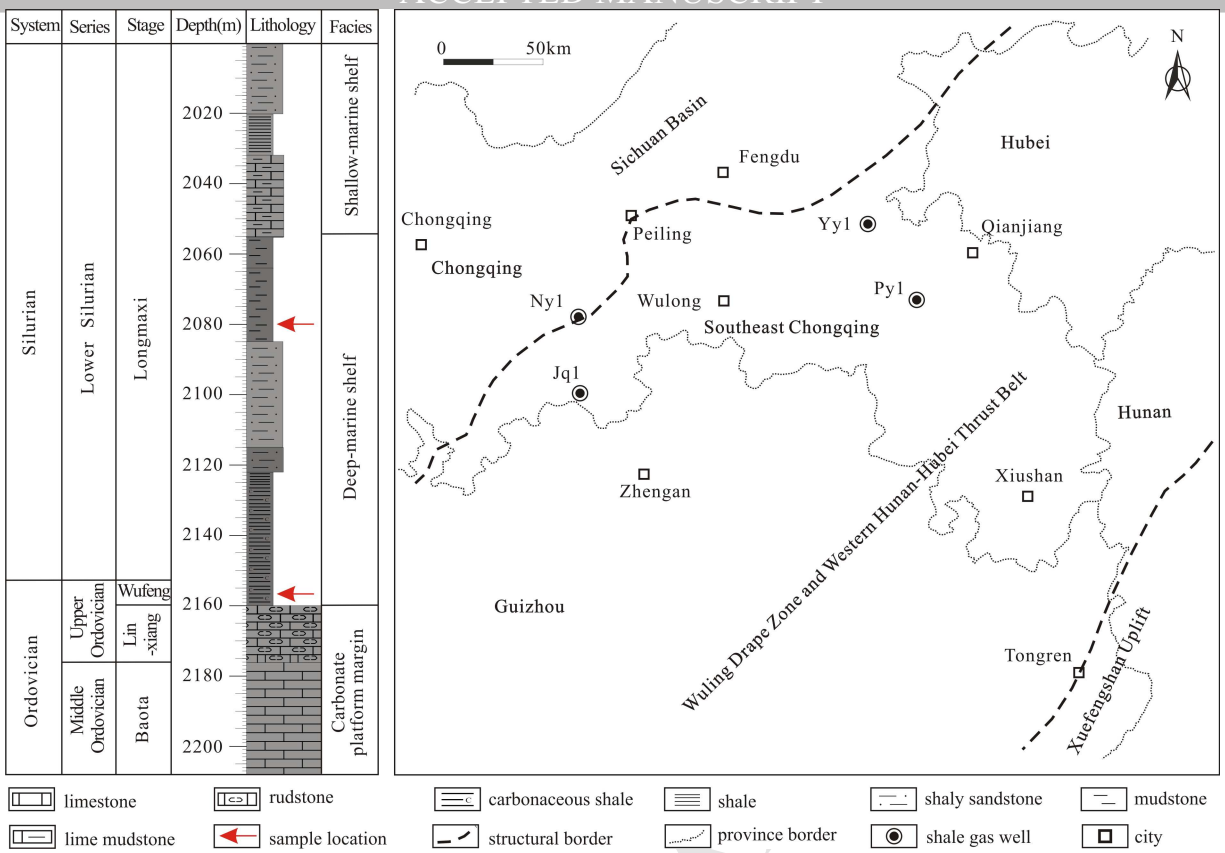

Fig. 1. The stratigraphic column of Py1 well and the location of Southeast Chongqing.

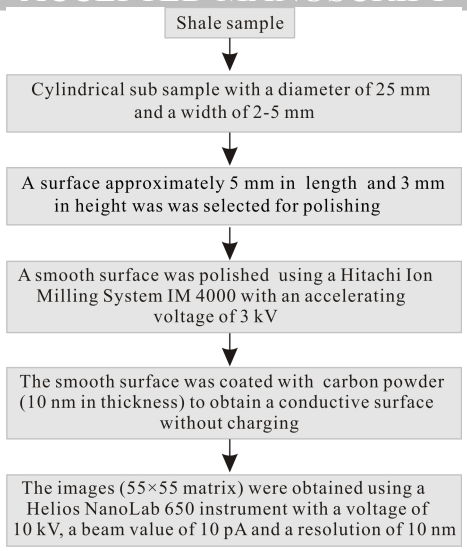

Fig. 2. The operating procedures of the SB-SEM experiment.

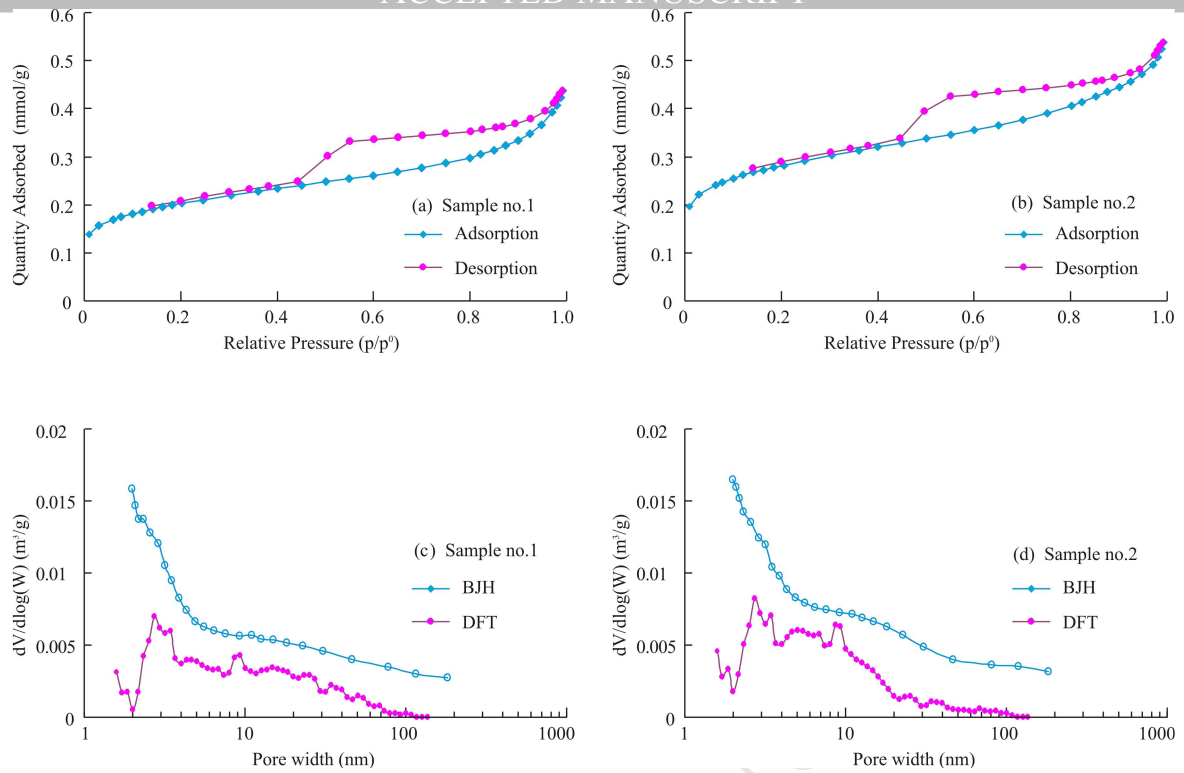

Fig. 3. Adsorption/desorption isotherms (a, b) and pore size distributions (c, d) calculated using the BJH and DFT models using the adsorption branch from the LTNA measurements.

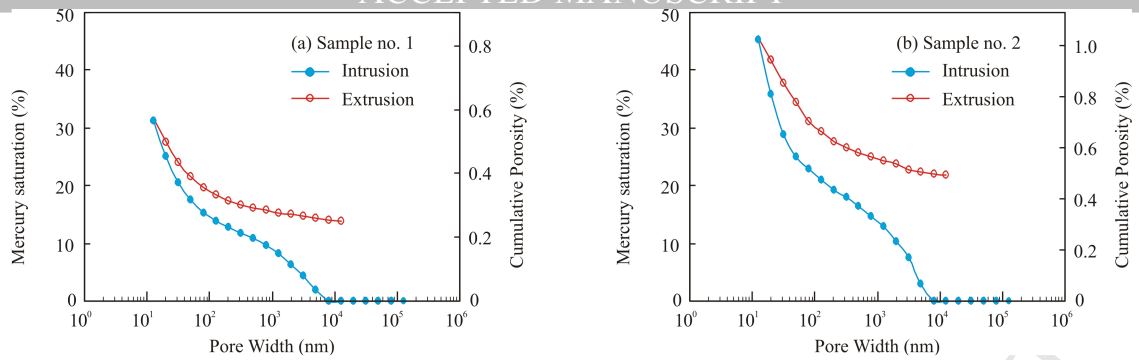

Fig. 4. The mercury saturation and cumulative porosity of intruded and extruded mercury curves from the MIP method.

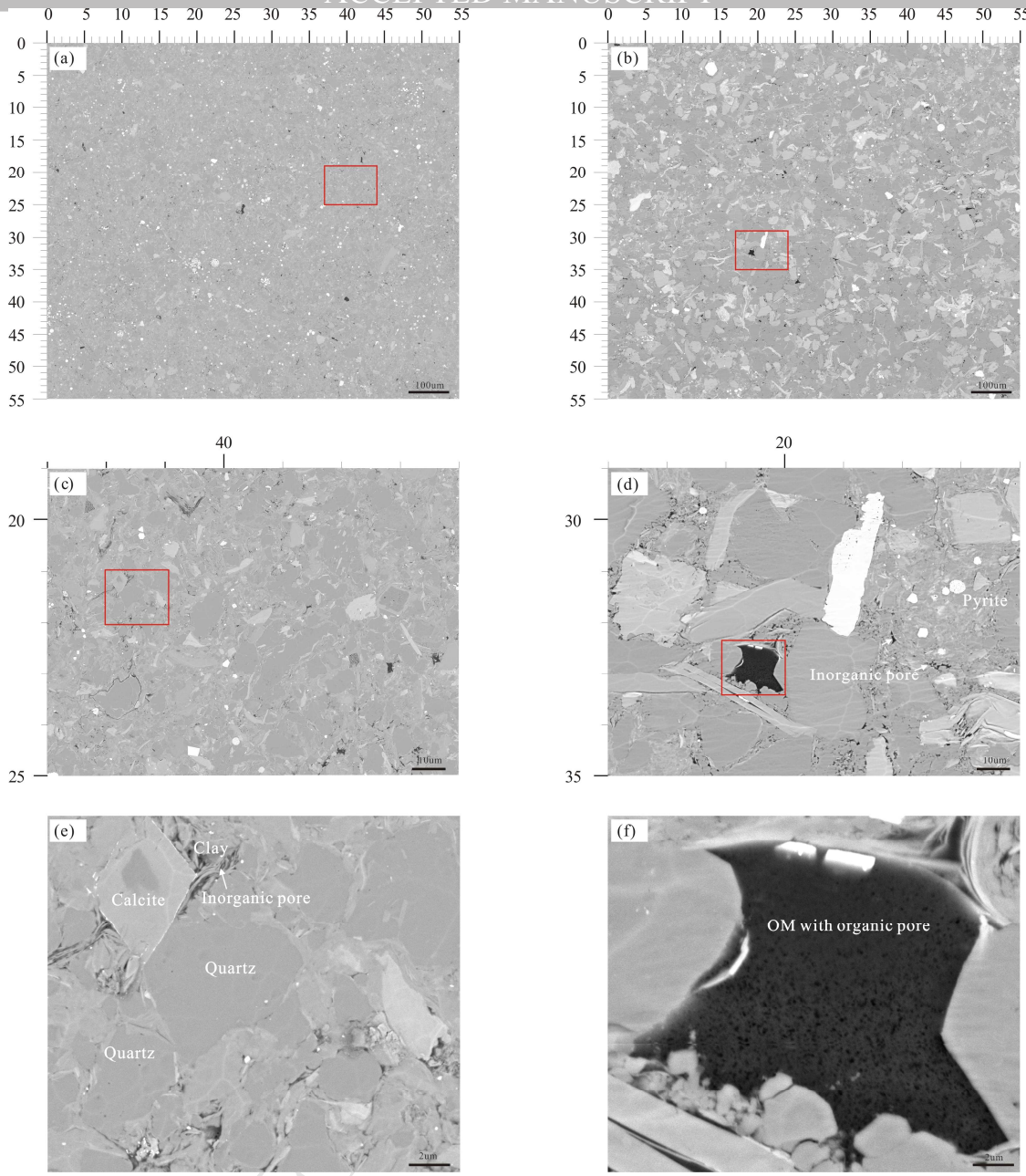

Fig. 5. The images of the Longmaxi Shale samples from Py1 well at multiple scales using the SB-SEM method. Figure a, c, and e show images from sample no. 1. Figure b, d and f show images from sample no. 2. Figure a and b are the composite images. Figure c and d are the local images, and the location is marked by a red rectangle in the composite images. Figure e and f are single scan images, and the location is marked by a red rectangle in the local images.

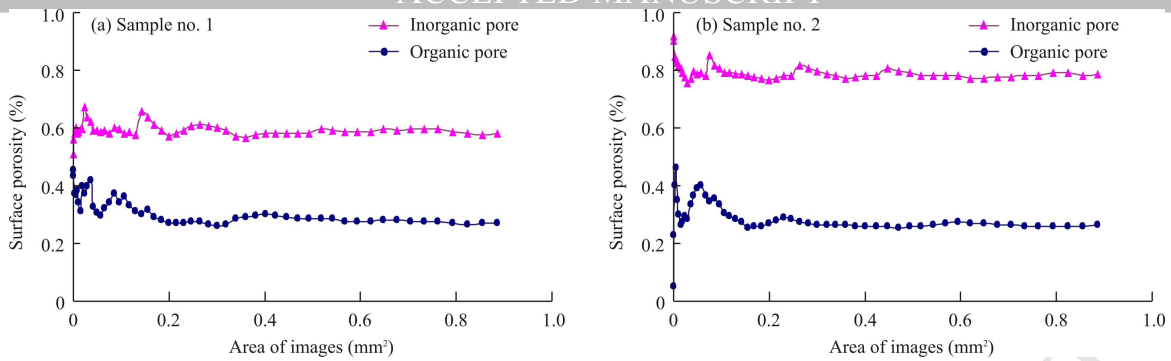

Fig. 6. The changes in organic and inorganic surface porosity with area, as determined from the SB-SEM images.

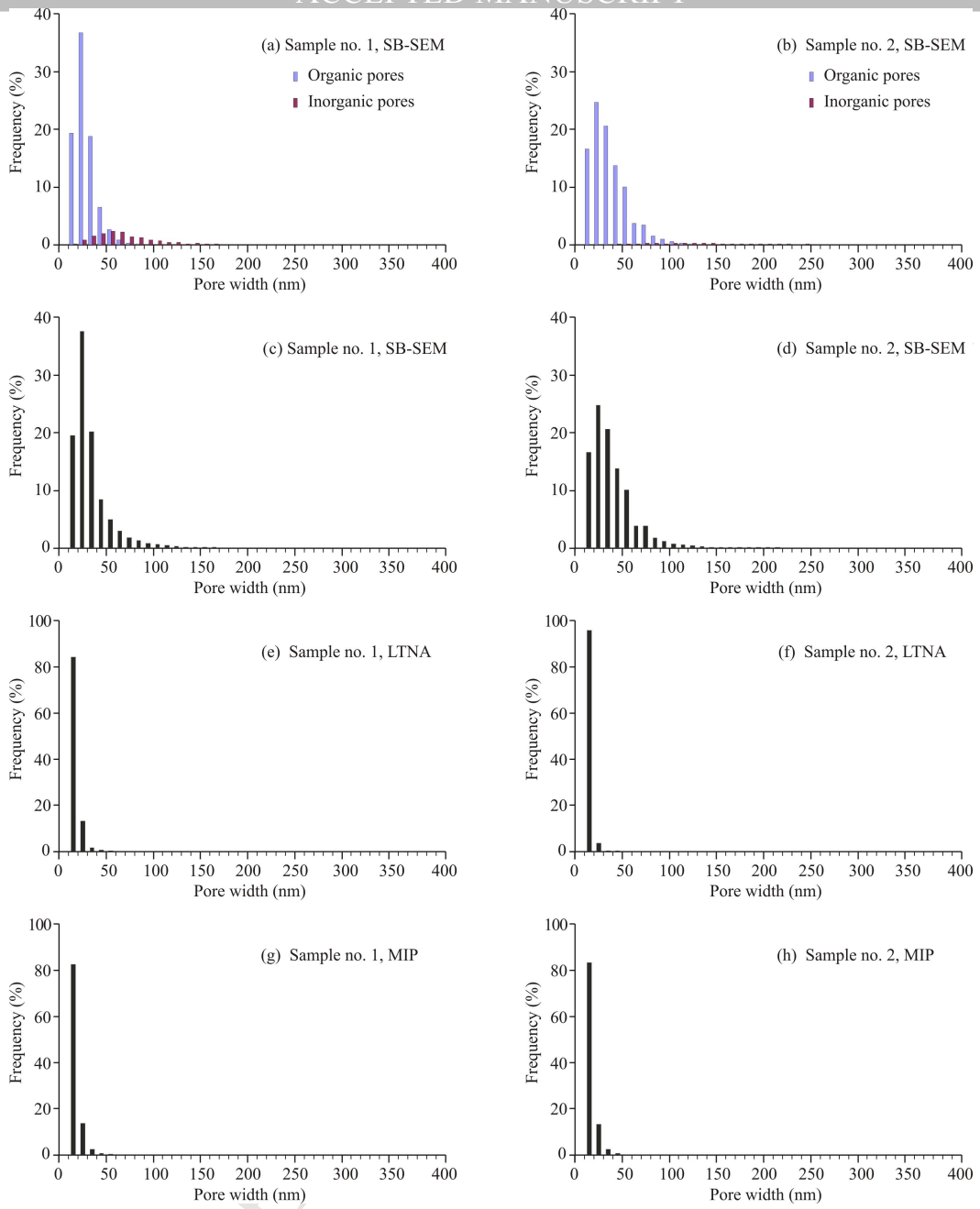

Fig. 7. The frequencies of pores with different pore widths obtained using the SB-SEM, LTNA and MIP methods. Panels a, b, c and d show the results from SB-SEM. Panels a and b show the frequencies of organic and inorganic pores for different pore widths. Panels c and d are the total frequencies of organic and inorganic pores for different pore widths. Panels e and f are the results from LTNA. Panels g and h show the results from MIP.

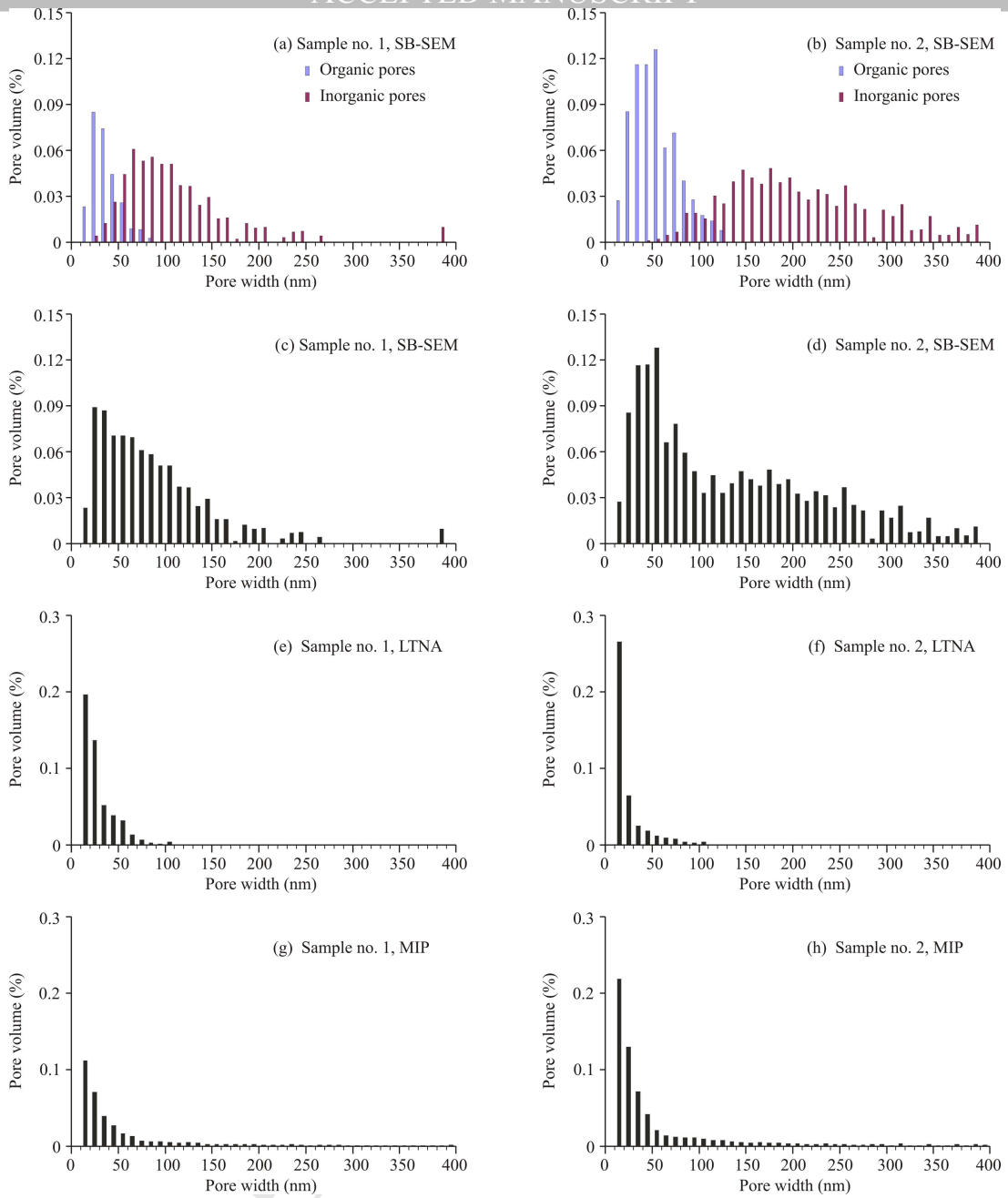

Fig. 8. The volumes of pores having different pore widths obtained using the SB-SEM, LTNA and MIP methods. Panels a, b, c and d show the results from SB-SEM. Panels a and b show the volumes of organic and inorganic pores with different pore widths. Panels c and d show the total volumes of organic and inorganic pores with different pore widths. Panels e and f show the results from LTNA. Panels g and h show the results from MIP.

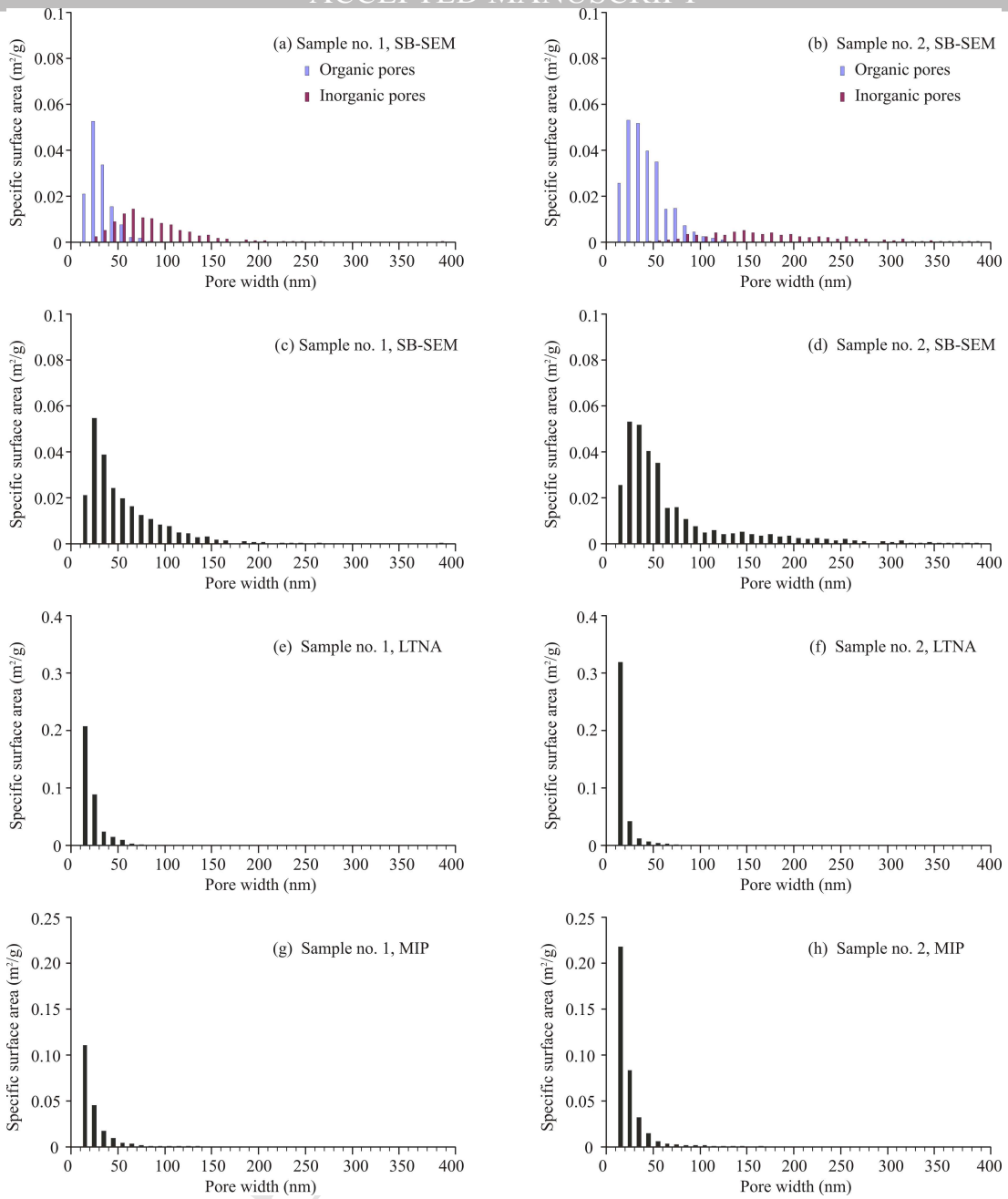

Fig. 9. The specific surface areas of pores with different pore widths obtained using the SB-SEM, LTNA and MIP methods. Panels a, b, c and d are the results from SB-SEM. Panels a and b are the organic and inorganic specific surface areas for different pore widths. Panels c and d are the total specific surface areas of organic and inorganic pores with different pore widths. Panels e and f are the results from LTNA. Panels g and h are the results from MIP.

Highlights

- The splicing of backscattered scanning electron microscopy method was introduced.
- The pore heterogeneity in shale sample decreases with increasing SB-SEM image area.
- The characteristics of pores in shale sample were evaluated by SB-SEM method.
- The results from SB-SEM were compared with those of LTNA and MIP methods.